IEEE Access
Multidisciplinary | Rapid Review | Open Access Journal

Received 30 June 2022, accepted 31 July 2022, date of publication 8 August 2022, date of current version 16 August 2022.

Digital Object Identifier 10.1109/ACCESS.2022.3197202

RESEARCH ARTICLE

Terahertz Beam Steering Using a MEMS-Based Reflectarray Configured by a Genetic Algorithm

XUAN LIU[1], LISA SCHMITT[2], BENEDIKT SIEVERT[3], (Member, IEEE), JONAS LIPKA[1], CHONG GENG[1], KEVIN KOLPATZECK[1], DANIEL ERNI[3], (Member, IEEE), ANDREAS RENNINGS[3], (Member, IEEE), JAN C. BALZER[1], (Member, IEEE), MARTIN HOFFMANN[2], AND ANDREAS CZYLWIK[1]

[1]Chair of Communication Systems, University of Duisburg-Essen, 47057 Duisburg, Germany
[2]Chair of Microsystem Technology, Ruhr-Universität Bochum, 44801 Bochum, Germany
[3]General and Theoretical Electrical Engineering (ATE), CENIDE—Center for Nanointegration Duisburg-Essen, Faculty of Engineering, University of Duisburg-Essen, 47048 Duisburg, Germany

Corresponding author: Xuan Liu (xuan.liu@uni-due.de)

This work was supported by the Deutsche Forschungsgemeinschaft (DFG), German Research Foundation, under Project 287022738-TRR 196, Project S01, Project C12, and Project C05.

ABSTRACT With the increase in potential uses of terahertz technology, the need for terahertz transceivers with application-oriented adaptive radiation patterns has emerged. Reconfigurable reflectarrays consisting of actuated sub-wavelength reflectors have been successfully used for terahertz beam steering and beamforming. They do not require a complex feeding network and associated electronics, enabling a compact and power-efficient terahertz beam steering system. However, the current reflectarray-based beam steering is accomplished by forming the reflectarray as a grating structure, which is accompanied by the problems such as grating lobes, limited steering range, and discrete steering angles. Here, we configure a MEMS-based reflectarray with the genetic algorithm to eliminate the grating lobes and open up the possibility of customizing its radiation pattern. We used single- and multi-objective optimization to find the optimal height profile of the reflectarray and verified the results by full-wave electromagnetic simulations. We measured the radiation patterns of four reflectarray phantoms, i.e. reflectarrays without the MEMS actuation systems. The measurement results agree well with the calculated ones, with the main beam deviating at most 2° from the target direction. Our work demonstrates how a genetic algorithm is used to shape a reconfigurable terahertz reflectarray to eliminate the grating lobes and tailor some specific featuress in its radiation pattern.

INDEX TERMS Beam steering, genetic algorithm, MEMS, optimization, reflectarray, terahertz.

I. INTRODUCTION

With the tremendous research efforts on terahertz systems, its great potential for wireless communication [1]–[3], sensing [4], [5], imaging [6]–[8], and spectroscopy [9]–[11] has been demonstrated. There are still challenges ahead for bringing the terahertz systems to the next level of maturity for the industry and commerce. According to the Friis transmission formula, the free space loss increases quadratically with frequency. In addition, the atmospheric absorption of terahertz radiation in a humid ambient condition is substantial [12], [13]. To ensure adequate receive power, we can use an antenna array to combine the power from multiple sources and at the same time achieve a high directivity. Moreover, an antenna array unlocks a fast scanning capability for terahertz systems, enabling real-time applications that can benefit sensing and imaging in a complex and large environment.

Over the past few decades, researchers have developed and advanced terahertz beam steering and beamforming techniques in various ways [14], [15]. The phased-array, as a mature concept at microwave frequencies, has been adapted to terahertz systems. In one implementation, the phase of each array element is shifted within the microwave band

The associate editor coordinating the review of this manuscript and approving it for publication was Michail Kiziroglou.

and the resulting phase shift is converted to the terahertz regime by frequency upconversion [16]–[18]. The advantage of such a terahertz phased-array is that the entire beamforming network prior to the frequency upconversion can be designed like a microwave phased-array. Nevertheless, a phase shifter [19]–[21] that can directly modulate the phase of the terahertz signal enables the compatibility with any terahertz source regardless of the generation methods. This subsequently simplifies the terahertz beamforming network.

Metasurfaces have attracted great attention in terahertz community and have been used in manipulating the terahertz wavefront by varying their geometrical parameters [26]–[28]. The leaky-wave antenna has been applied to steer the terahertz beam by changing the operating frequency [22]–[24]. This working principle has an intrinsic drawback: the steering of the main beam direction is always accompanied by a change in frequency. To control the beam direction and the frequency independently, Esquius-Morote *et al.* [25] proposed the concept of a modulated graphene leaky-wave antenna for terahertz beam steering at a fixed frequency.

Spatial modulation is another phase shifting technique that is often used in terahertz beam steering and beamforming network. Preu *et al.* [29] and Maki and Otani [30] have successfully demonstrated the control of the terahertz beam direction by spatially modulating the optical signal that is used for the terahertz generation. The resulting phase shift is translated into the terahertz domain after difference frequency generation or photomixing. Due to the sub-mm wavelength in the terahertz regime, spatial modulation of terahertz waves is feasible in both transmission and reflection mode. In transmission mode, a photo-active semiconductor can be placed in the terahertz channel. Once the semiconductor is illuminated by a spatially modulated optical pump, a photo pattern (e.g. blazed grating pattern) is induced. The terahertz wave is spatially modulated as it passes through the semiconductor [31]–[34]. In reflection mode, the beam steering can be done by a reflectarray that consists of multiple actuated sub-wavelength reflectors [35]–[37].

Among the terahertz beam steering and beamforming techniques described above, the reflectarray is a promising candidate for a compact, simple, and power-efficient terahertz beam steering network compatible with any terahertz source. The reflectarray does not require a complex feeding network and associated electronics, drastically reducing the design and technological complexity. Furthermore, it can achieve pure phase modulation without simultaneously modulating the amplitude of the reflected wave. In the work by Monnai *et al.* [35], the reflectarray is formed as a grating structure and the reflected terahertz beam is steered in different directions by varying the grating period of the reflectarray. However, the reflectors with only a binary state lead to inefficient diffraction, which results in the beam being diffracted mainly normal to the grating.

In our previous work [38], we presented a mathematical model to calculate the radiation pattern of a reflectarray that shifts the phase of the terahertz beam by adjusting the height

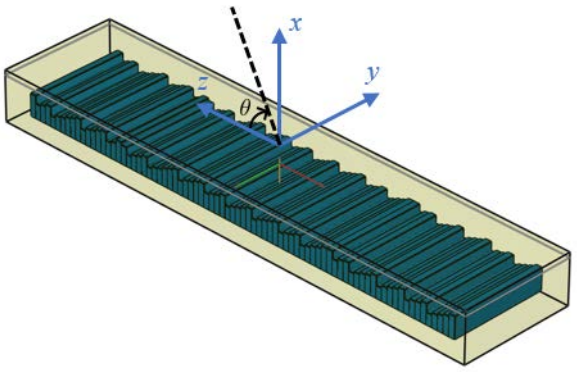

FIGURE 1. EM simulation setup in EMPIRE XPU. The reflectarray (in blue color) is enclosed in a plane wave box (yellow box). The far-field monitor is placed on the *xz*−plane to record the scattered field of the reflectarray.

of each reflector individually. We arranged the reflectarray to approximate a blazed grating structure, steering the beam by varying its grating period. This approximate blazed grating structure has major grating lobes in its radiation pattern, normal to the grating and opposite the main beam. It also has a limited angular range and low angular resolution as the grating period can only be an integer multiple of the reflector width. In this work, we use a genetic algorithm (GA) to optimize the radiation pattern of the reflectarray, providing a non-perfect periodic structure that eliminates the grating lobes. The resulting reflectarray also has a wider angular range and a finer angular resolution. In addition, we can manipulate the characteristics of the radiation pattern of the reflectarray in a way that is not possible using a grating structure.

The rest of this paper is organized in six sections. In Section II, we describe the single-objective optimization problem for the MEMS-based reflectarray, presenting the design variables, the conditions that the design variable must satisfy, and three optimization objectives and their corresponding GA fitness functions. The three optimization objectives are: maximizing the directivity in the target direction, minimizing the sidelobe level, and nulling at a given angle. We then perform the Fourier transform of the reflectarray structure obtained by the GA to interpret its spatial periodicity. In Section III, we observe the conflicting behavior between the first two optimization objectives and perform a multi-objective GA to give the Pareto front. Section IV describes the MEMS actuation system and the MEMS-reflectarray structure in detail. As a proof of concept, we carry out planar and 3D radiation pattern measurements of four reflectarray phantoms, i.e. reflectarrays without the MEMS actuation systems. Section V presents the design of the reflectarray phantoms, radiation pattern measurement setup, results, and discussions. At last, we conclude with a summary of our work in Section VI.

II. SINGLE-OBJECTIVE OPTIMIZATION

Most terahertz applications require at least one of the following radiation pattern characteristics: maximized directivity in

TABLE 1. Options for the single-objective GA.

Size of the population	200
Creation of the initial population	The initial population is created with a uniform distribution
Stopping criteria	Average cumulative change in value of the fitness function over 50 generations is less than 10^{-6}
Maximum number of generations	8000
Number of elite	10
Mutation option	Gaussain
Crossover option	Scattered

an arbitrary direction to compensate for low transmit power and high atmospheric absorption, minimized sidelobe level, or a steerable null to mitigate an interferer. Obtaining the radiation pattern of the reflectarray with the desired characteristics can be considered as an optimization problem. The desired characteristics are the optimization goals, and the heights of the reflectors are the design variables.

We consider a reflectarray consisting of 80 identical rectangular reflectors. The reflectors have a reflective surface of 300 μm x 5000 μm and are arranged adjacent to each other on their long sides. Each reflector has an independent 5-bit MEMS actuation system, allowing a maximum vertical displacement of 600 μm. The design variables: the heights of the 80 reflectors are bounded between 0 to 600 μm with no other constraints. Note that the reflectors can only stay in 2^5 vertical positions. First, we neglect the discretization and solve the continuous optimization problem. After finding the optimal heights of the reflectors, we round them to the closest feasible positions. To verify the optimization results, we perform full-wave electromagnetic (EM) simulations of the obtained reflectarray using the finite-difference time-domain solver EMPIRE XPU. A plane wave box is used for the plane wave excitation. A fictitious current flows on the surfaces of the plane wave box such that both the incident and scattered fields are present inside the box, while only the scattered field is present outside the box. As shown in Fig.1, the reflectarray is enclosed by the plane wave box. The simulation boundary with absorbing boundary conditions is at a distance from the plane wave box of two times the wavelength of the target simulation frequency. The simulation area is meshed according to the following rules: at least 4 cells per object dimension and at least 15 cells per wavelength of the highest simulation frequency. A far-field monitor is defined on the $xz-$plane to record the scattered field of the reflectarray.

In this section, we use a GA implemented in MATLAB to solve the optimization problem and discuss single-objective optimizations for three objectives: maximizing the directivity, minimizing the sidelobe level, and nulling at a given angle. For each single-objective optimization, we describe its optimization goal with one or multiple fitness functions. In addition, we numerically compare the multiple fitness functions to select which one of them best fits the optimization objective.

TABLE 2. Averaged directivity D_{avg}, sidelobe level SLL_{avg}, 3 dB beamwidth θ_{3dB}, runtime t_{avg}, and standard deviation σ over 20 optimization runs using the enlisted fitness functions.

	$f_{\text{D},1}$	$f_{\text{D},2}$	$f_{\text{D},3}$
D_{avg}	16.78 dBi	16.82 dBi	16.67 dBi
SLL_{avg}	-12.96 dB	-13.10 dB	-12.79 dB
θ_{3dB}	2.97°	2.98°	2.97°
t_{avg}	7 min	126 min	3 min
σ	0.066 dB	0.044 dB	0.063 dB

A. MAXIMIZING DIRECTIVITY

We propose three different fitness functions for the single-objective optimization to maximize the directivity $D(\theta = \theta_{\text{desired}})$ in the desired direction θ_{desired}. The first proposed fitness function is the reciprocal of the directivity $D(\theta = \theta_{\text{desired}})$:

$$f_{\text{D},1} = \frac{1}{D(\theta = \theta_{\text{desired}})}. \tag{1}$$

The goal of this fitness function is to maximize the directivity $D(\theta = \theta_{\text{desired}})$ in the desired direction without having to satisfy any predefined target value.

For the other two fitness functions, we take a uniform linear array of point-source isotropic radiators as a reference. Its directivity at the desired angle $D_{\text{ULA}}(\theta = \theta_{\text{desired}})$ is the target value that $D(\theta = \theta_{\text{desired}})$ needs to meet. The uniform linear array has the following parameters:

- The overall length l of the uniform linear array is the same as that of the MEMS-based reflectarray: $l = 80 \cdot 300\,\mu\text{m} = 24\,\text{mm}$.
- The element spacing d of the uniform linear array is less than half of the wavelength at the design frequency.

We define the other two fitness functions as:

$$f_{\text{D},2} = \left(D(\theta = \theta_{\text{desired}}) - D_{\text{ULA}}(\theta = \theta_{\text{desired}})\right)^2 \text{ and} \tag{2}$$

$$f_{\text{D},3} = 1 - \exp\left(-\frac{\left(D(\theta = \theta_{\text{desired}}) - D_{\text{ULA}}(\theta = \theta_{\text{desired}})\right)^2}{2 \cdot (240)^2}\right), \tag{3}$$

so that $f_{\text{D},2} = f_{\text{D},3} = 0$ when $D(\theta = \theta_{\text{desired}}) = D_{\text{ULA}}(\theta = \theta_{\text{desired}})$.

We carry out three independent runs of the GA with fitness function (1), (2), and (3), respectively. The optimization goal is to maximize the directivity in the direction of 45° at 300 GHz. The parameters of the GA are listed in Table 1 and remain unchanged for all three runs. The calculated and the EM simulated radiation patterns of the obtained reflectarrays are depicted in Fig. 2. With all three fitness functions, the main beam is successfully steered to 45° with a directivity of approx. 16.7 dBi and sidelobe level of −13 dB.

Due to its intrinsic randomness, a GA returns different optimal results for each execution despite using the same machine, fitness function, optimization objective, and parameter settings. Therefore, to fairly compare these three fitness functions, we run the GA 20 times with each fitness

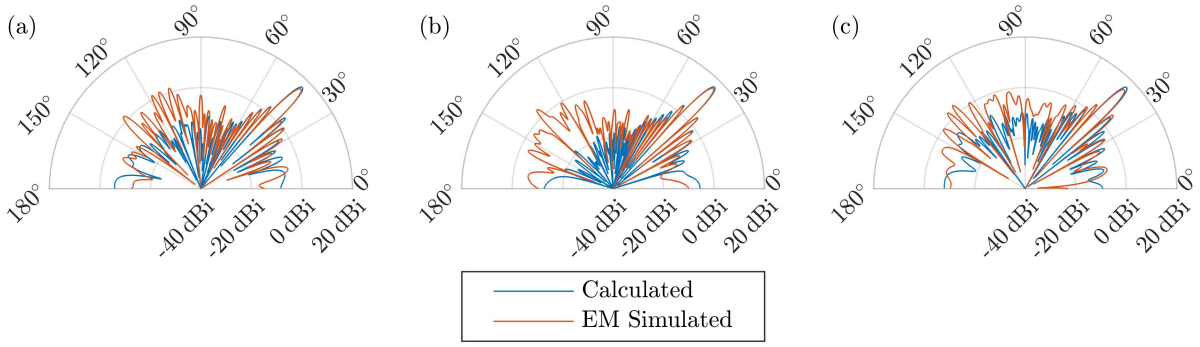

FIGURE 2. Calculated (in blue color) and EM simulated (in red color) radiation patterns of the reflectarray obtained by the GA with the fitness functions (a) $f_{D,1}$, (b) $f_{D,2}$, and (c) $f_{D,3}$, respectively.

function and summarize the averaged directivity D_{avg}, sidelobe level SLL_{avg}, 3 dB beamwidth $\theta_{3\text{dB}}$, runtime t_{avg}, and the standard deviation σ of the 20 resulting directivities in the target direction in Table 2. The resulting directivities using the three fitness functions are similar. The fitness function $f_{\text{D},2}$ performs slightly better in terms of averaged directivity and standard deviation. However, it takes much longer to converge compared to the other two fitness functions.

B. MINIMIZING SIDELOBE LEVEL

In this subsection, we define and compare three different fitness functions for minimizing the sidelobe level. The first proposed fitness function $f_{\text{SLL},1}$ is:

$$f_{\text{SLL},1} = \frac{\max\left(D\left(\theta \neq \theta_{\text{desired}}\right)\right)}{D\left(\theta = \theta_{\text{desired}}\right)}. \tag{4}$$

It minimizes the ratio of the directivity of the highest side lobe to the directivity of the main lobe and works without knowing the target sidelobe level.

The second fitness function $f_{\text{SLL},2}$ is defined by the mask-based method proposed by Sheikholeslami and Atlasbaf [39]. The masks that are used for the fitness function $f_{\text{SLL},2}$ are shown in Fig. 3(a). The shape of the upper mask $M_{\text{up}}(\theta)$ and the lower mask $M_{\text{down}}(\theta)$ determines the key features of the target radiation pattern:

- θ_{mb} defines angle difference between the diametrically opposed nulls around the maximum peak
- θ_{HPBW} defines the half-power beam width
- SLL_{t} determines the target sidelobe level.

The fitness function is defined as follows [39]:

$$\begin{aligned} f_{\text{fitness}} &= \left(M_{\text{up}}^2(\theta) - \frac{D(\theta)}{D(\theta_{\text{desired}})}\right) \cdot \left(M_{\text{down}}^2(\theta) - \frac{D(\theta)}{D(\theta_{\text{desired}})}\right) \\ &\quad + \left|M_{\text{up}}^2(\theta) - \frac{D(\theta)}{D(\theta_{\text{desired}})}\right| \cdot \left|M_{\text{down}}^2(\theta) - \frac{D(\theta)}{D(\theta_{\text{desired}})}\right|. \end{aligned} \tag{5}$$

Once the radiation pattern completely lies within the area bounded by the upper and lower masks, the fitness function $f_{\text{SLL},2}$ reaches its minimum $f_{\text{SLL},2} = 0$.

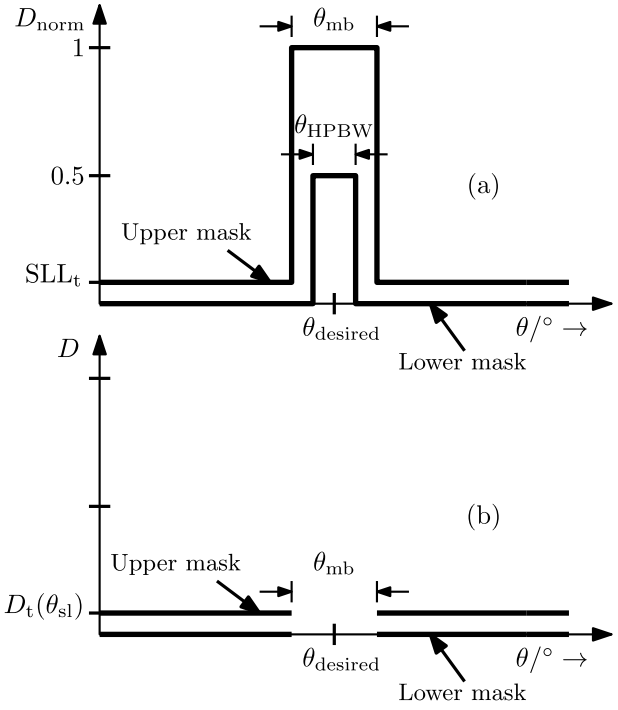

FIGURE 3. Masks used to restrict the radiation pattern in fitness function (a) $f_{\text{SLL},2}$ and (b) $f_{\text{SLL},3}$.

The third fitness function $f_{\text{SLL},3}$ is defined by adapting the mask-based method and assigning an absolute value to the maximum directivity of the side lobes $D_{\text{t}}(\theta_{\text{sl}})$ as shown in Fig. 3(b). We exclude the main beam characteristics by leaving a gap around the target direction with the width of θ_{mb}.

We first carry out three independent runs of the GA with the fitness functions $f_{\text{SLL},1}$, $f_{\text{SLL},2}$, and $f_{\text{SLL},3}$, respectively. The incident wave on the reflectarray has a frequency of 300 GHz. The following values are assigned to the mask variables for the optimization:

- $\theta_{\text{mb}} = 6°$
- $\theta_{\text{HPBW}} = 3°$
- $\theta_{\text{desired}} = 45°$

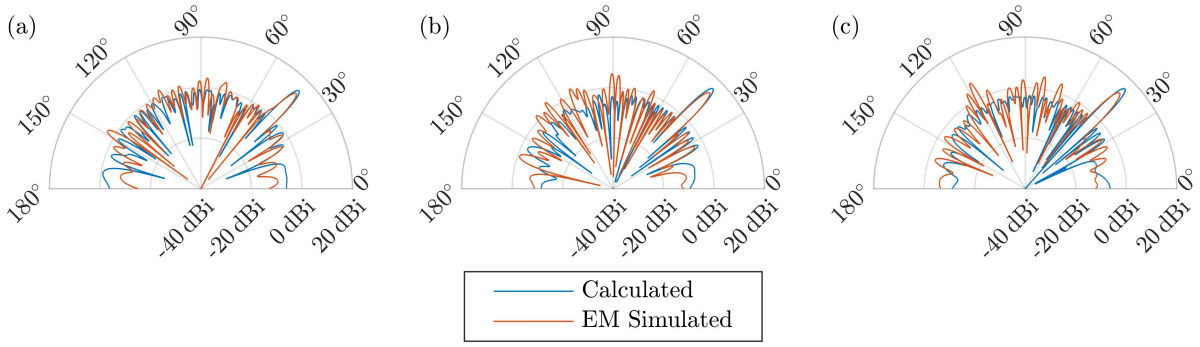

FIGURE 4. Calculated (in blue color) and EM simulated (in red color) radiation patterns of the reflectarray obtained by the GA with the fitness functions (a) $f_{\text{SLL},1}$, (b) $f_{\text{SLL},2}$, and (c) $f_{\text{SLL},3}$, respectively.

TABLE 3. Averaged directivity D_{avg}, sidelobe level SLL_{avg}, 3 dB beamwidth $\theta_{3\text{dB}}$, execution time t_{avg}, and standard deviation σ over 20 simulation runs carried out by GA using the enlisted fitness functions.

	$f_{\text{SLL},1}$	$f_{\text{SLL},2}$	$f_{\text{SLL},3}$
D_{avg}	14.44 dBi	15.83 dBi	15.71 dBi
SLL_{avg}	-14.08 dB	-17.51 dB	-18.4 dB
$\theta_{3\text{dB}}$	3.15°	3.08°	3.1°
t_{avg}	12 min	40 min	130 min
σ	0.97 dB	0.26 dB	0.2 dB

- $\text{SLL}_{\text{t}} = -18\,\text{dB}$
- $D_{\text{t}}(\theta_{\text{sl}}) = -3\,\text{dBi}$.

Fig. 4 shows the calculated and EM simulated radiation patterns of the obtained reflectarrays. The side lobes, especially around the main lobe, are significantly suppressed. As in Section II-A, we run the GA 20 times with each fitness function and summarize the averaged directivity D_{avg}, sidelobe level SLL_{avg}, 3 dB beamwidth $\theta_{3\text{dB}}$, runtime t_{avg}, and the standard deviation σ of the 20 resulting sidelobe levels in Table 3. Comparing this with the results presented in Table 2, we see that the sidelobe level is significantly reduced. However, we observe a degradation in the directivity. The fitness function $f_{\text{SLL},3}$ provides the best performance, which has the minimum sidelobe level at the cost of longer runtime.

C. NULLING IN A SPECIFIC DIRECTION

To achieve nulling in the interferer direction while the main beam is steered to the target angle, we define the fitness function using the equally weighted sum method:

$$f_{\text{null}} = \frac{1}{D\left(\theta = \theta_{\text{desired}}\right)} + D\left(\theta = \theta_{\text{nulling}}\right). \tag{6}$$

This fitness function combines the two optimization objectives of maximizing the directivity in the target direction and nulling in the interferer direction. We carry out two independent runs of the GA with the fitness function f_{null}, nulling at $\theta_{\text{nulling}} = 20°$ and $\theta_{\text{nulling}} = 30°$, respectively. For these two optimizations, the incident wave on the reflectarray has a frequency of 300 GHz and the main beam is kept at $\theta_{\text{desired}} = 45°$. As depicted in Fig. 5, both calculated and EM simulated radiation patterns show that the null is successfully shifted from 20° to 30°, while the main beam remains at 45°.

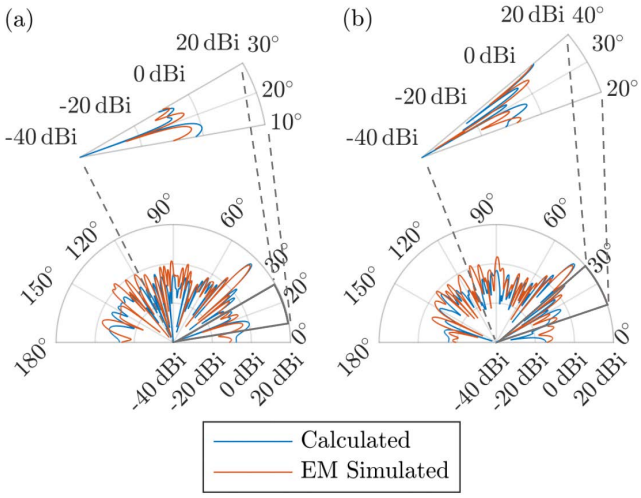

FIGURE 5. Calculated (in blue color) and EM simulated (in red color) radiation patterns of the reflectarray obtained by the GA with the fitness function f_{null}, nulling at (a) $\theta = 20°$ and (b) $\theta = 30°$, respectively.

D. REFLECTARRAY CONFIGURED BY GA VS. GRATING STRUCTURE

The optimization results presented in Section II-A – II-C prove the feasibility of using the GA to optimize such a reflectarray. In this subsection, we take a close look at the height profile of the resulting reflectarray and compare its radiation pattern with the radiation pattern of a grating structure.

The heights of the 80 reflectors of an optimized reflectarray are depicted in Fig. 6. This reflectarray is obtained by a single-objective GA with the fitness function $f_{\text{D},1}$. The optimization objective is to maximize the directivity at 33.6° away from the grating surface at 300 GHz. The height profile of the reflectarray is a saw-tooth structure with varying periods. We calculate the Fourier transform of the structure to interpret its periodicity in space. As shown in Fig. 7, there is a

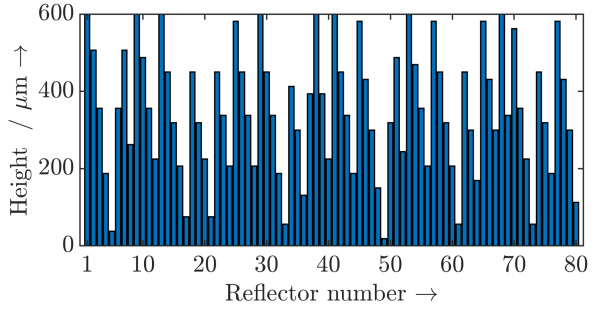

FIGURE 6. Heights of the 80 reflectors of the reflectarray obtained by the GA.

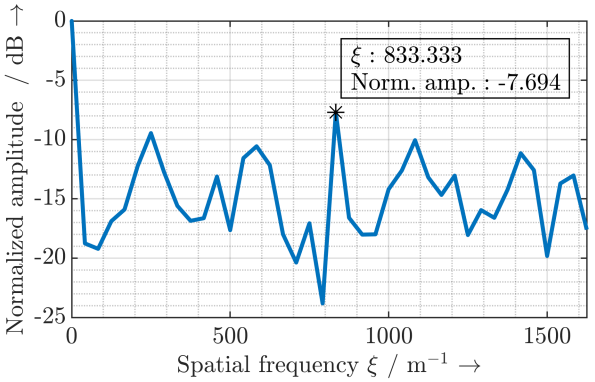

FIGURE 7. Fourier transform of the structure shown in Fig. 6.

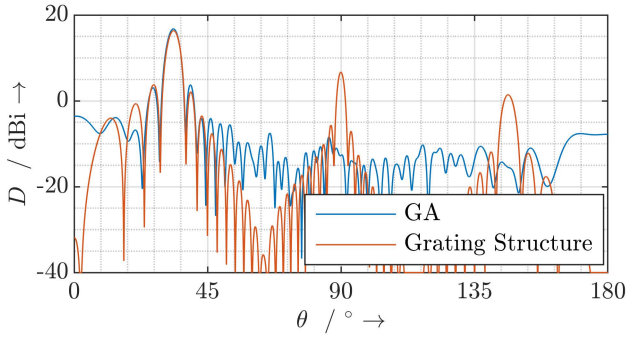

FIGURE 8. Calculated radiation patterns of the reflectarray structure obtained by GA (in blue color) and the grating structure (in red color).

dominant spatial frequency component at $\xi = 833.333\,\mathrm{m}^{-1}$. Its reciprocal is the period in space $\Lambda = \xi^{-1} = 1.2\,\mathrm{mm}$. By inserting the period Λ into the grating equation, we obtain a first-order diffraction angle of 56.4°, whose complementary angle is our desired angle of 33.6°. This indicates that the reflectarray obtained by the GA is a grating structure with a non-perfect period. As illustrated in Fig. 8, the non-perfect periodicity results in the elimination of the grating lobes at the normal of the reflectarray and opposite to the main beam. This makes the reflectarray obtained by the GA superior to a conventional grating structure.

III. MULTI-OBJECTIVE OPTIMIZATION

By comparing Table 2 and Table 3, we note the trade-off between the two objectives of maximizing the directivity and

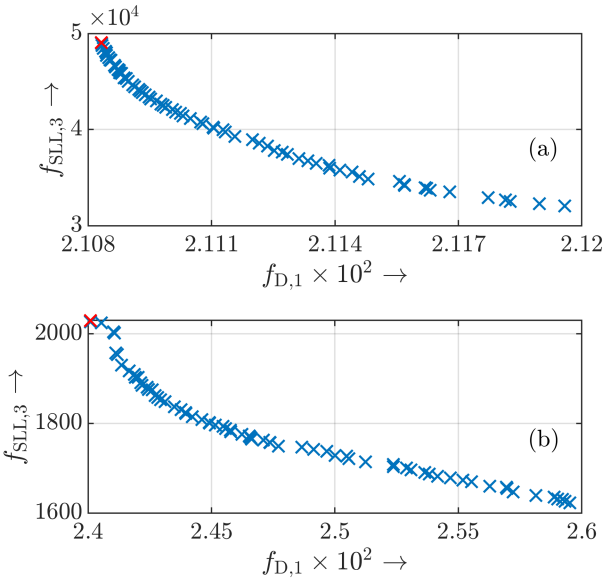

FIGURE 9. Pareto front given by the multi-objective GA with the initial population being the output of the single-objective GA with the objective of (a) maximizing the directivity and (b) minimizing the sidelobe level.

minimizing the sidelobe level: the result of one cannot be improved without degrading results of the other. For such an optimization problem involving two conflicting objectives, multi-objective optimization can be used to produce the optimum sets of the two objectives. In this section, we consider applications that require both high directivity and low sidelobe level by performing a multi-objective optimization and obtaining its Pareto-optimum front, which shows the trade-off and gives the optimum sets of the objectives.

The design variables of the multi-objective optimization are the same as in the single-objective GA. The optimization objectives are maximizing the directivity in the direction of 45° at 300 GHz and minimizing the sidelobe level. We describe these two objectives by the fitness function $f_{D,1}$ and $f_{SLL,3}$, respectively. The values assigned to the mask variables are the same as in Section II-B. After experimenting with different ways to implement the multi-objective GA, we realize that it has the best performance when its initial population is the output of a single-objective GA.

Fig. 9 shows two Pareto fronts, which are obtained by carrying out two independent runs of the multi-objective GA. Fig. 9(a) depicts the Pareto set output by the multi-objective GA with its initial population being the output of the single-objective GA whose optimization objective is to maximize the directivity. Fig. 9(b) depicts the Pareto set output by the multi-objective GA with its initial population being the output of the single-objective GA whose optimization objective is to minimize the sidelobe level. By comparing these two Pareto sets, we identify that the initial population governs the focus of the optimization objectives. The Pareto set in Fig. 9(a) has a smaller value of $f_{D,1}$ and therefore higher directivity, whereas the Pareto set in Fig. 9(b) has a smaller value of $f_{SLL,3}$ and therefore a lower sidelobe level. Let us

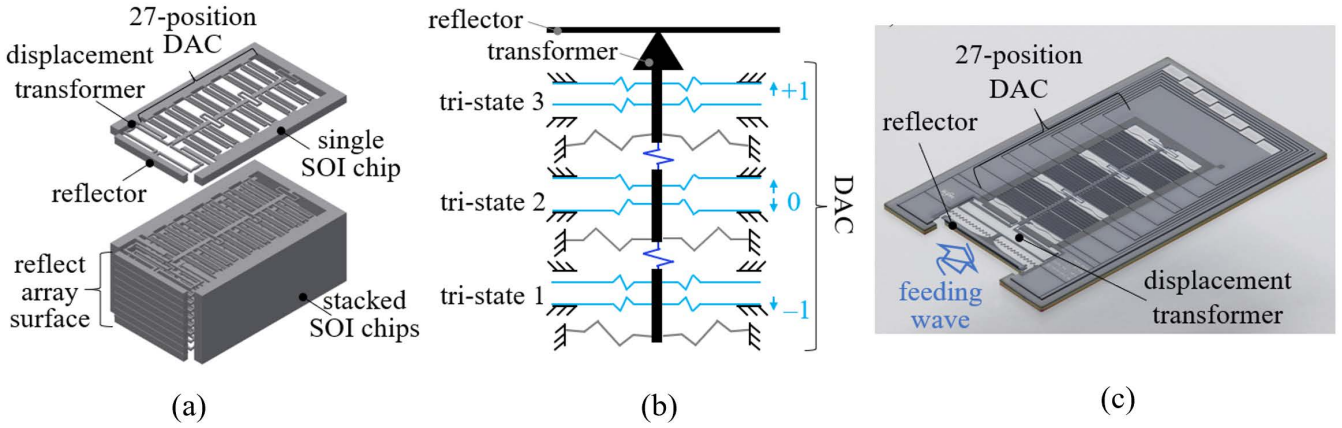

FIGURE 10. (a) Drawing of the reflectarray. (b) Schematic of the 27 position DAC exemplarily in position (+1 0 −1) as the tri-state 1 is in position −1, the tri-state 2 is in position 0, and the tri-state 3 is in position +1. (c) Stacked Photo of a fabricated single SOI chip.

now compare the optimal results given by the multi-objective GA and the single-objective GA. The tagged element in red color in Fig. 9(a) has a maximum directivity of 16.76 dBi and a sidelobe level of -14.2 dB. Comparing these results to those in the second column of Table 2, the multi-objective GA achieves the same level of the directivity but with a lower sidelobe level. The tagged element in red color in Fig. 9(b) has a maximum directivity of 16.19 dBi and a sidelobe level of -18.59 dB. The multi-objective GA improves the directivity in addition to returning almost the same sidelobe level compared with the single-objective GA results in the fourth column of Table 3.

IV. MEMS-BASED REFLECTARRAY

In Section II and III, the optimization is carried out based on a 5-bit MEMS actuation system that allows a maximum vertical displacement of 600 μm. As a preliminary work, we successfully demonstrated a 3-bit MEMS actuator supporting a maximum throw of 151.3 μm [40]. To reduce the wirebonding complexity that drastically increases with the number of the reflectors, we stack five MEMS-based reflectors on one substrate and then place the stacks next to each other. However, this arrangement results in a gap between the stacks with a thickness of the substrate. In the first part of this section, the structure of the reflectarray and the essential actuation mechanism are described in detail. In the second part of this section, we propose an alternative reflectarray design by filling the gaps with static reflectors to reduce the effects that the gaps have on the radiation pattern.

A. HIGH-THROW AND MULTI-STABLE MEMS

A schematic structure of the reflectarray is shown in Fig. 10(a). The reflectarray consists of several single silicon-on-insulator (SOI) chips stacked together. Each SOI chip features a reflector and an actuator system consisting of a 3^3-position digital-to-analog converter (DAC) and a mechanical displacement transformer. The actuator system and the reflector are made from a single SOI substrate. The application of the reflectarray in the terahertz regime sets the demands on the SOI chips. First, the reflector needs to feature a large surface. In addition, the actuator system has to perform a stepwise discrete and large displacement of the reflector.

Performing large displacements with multipoint stability has been a topic of research for quite a long time. Comb-drive actuators have been investigated for large displacements [41]–[43] and are getting more of interest for photonic and terahertz applications as well [44], [45]. In our previous work [46], an in-plane actuator system is presented consisting of multiple bending-plate actuators that generate a stepwise actuator displacement up to 230.7 μm $\pm$ 0.9 μm at 54 V. Thus, the number of conducting paths is equal to the number of actuators resulting in complex control circuits. Therefore, solutions with DACs appear as a promising alternative. For DACs, the number of positions increases with the number of actuators N by the factor $2N$. Such DACs are e.g. presented in [47]–[49] using thermal or electrothermal actuation. As terahertz reflectarrays require a high precision positioning and quick response times, electrostatic actuators are a good solution. In [50] and [51] it is shown that DACs based on comb-drive actuation can achieve a large binary encoded displacement at a low voltage.

We have presented a DAC based on bending-plate actuators [40]. As depicted in Fig. 10(b), this DAC is comprised of three tri-states combined by connecting springs. Each tri-state features two actuators and can approach three positions. The DAC exemplarily shown in Fig. 10(b) is in position (+1 0 −1) as the tri-state 1 is in position −1 by only activating the downwards actuator, the tri-state 2 is in position 0 by activating both actuators at once, and the tri-state 3 is in position +1 by activating only the upwards actuator. With this setup, the DAC addresses up to $3^3 = 27$ positions and generates a discrete and small displacement. This small displacement is increased by the mechanical transformer [52] and conducted to the reflector. The fabrication process allows

the design of the reflectors with a large surface. Whereas the actuator system is only fabricated on the (thin) device layer, the reflector surface consists of the combined device and (thick) handle layer resulting in a large reflector surface. This design solution was presented in [53] and also allows the removal of the SOI frame in front of the reflector to have an open interface for the feeding wave as depicted in the stacked device photo of a single fabricated SOI chip in Fig. 10(c). During fabrication, the handle layer from behind the actuators is removed, so that the single SOI chips can be stacked without an additional intermediate layer resulting in a minimum gap between each reflector.

As shown in Fig. 10(a), the single chips are stacked to a reflectarray. For stacking, the chips have to increase in length so that each bond pad placed underneath the actuators (Fig. 10(c)) is accessible for the bond wire. Despite each chip only requires seven bond pads for 27 positions, the number of bond wires and the chip length increases with the number of stacked chips so that a direct stacking of many chips is not possible. As a solution, we propose to compose the array by groups of five chips on one printed circuit board (PCB).

B. STATIC REFLECTORS

Forming the reflectarray by stacking the groups of five MEMS-based reflectors together results in a gap between the adjacent stacks. To accommodate the substrate to which the reflectors are attached, the thickness of the gap must be at least equal to the thickness of the substrate. We consider a gap with the thickness of 300 μm, which is the PCB fabrication manufacturer's standard substrate thickness. Note that 300 μm is also the width of the reflector. Thus, a reflectarray with the reflective surface of 24 mm $\times$ 5 mm consists of 67 MEMS-based reflectors and 13 gaps. Due to the relatively low permittivity of the PCB substrate, the incident beam reflects weaker on the PCB substrate surface than on the silicon substrate used for the reflectors. Now, we fill these gaps with the reflectors without actuation systems: static reflectors. The reflective surface of each static reflector is 300 μm $\times$ 5000 μm, just like the MEMS-based reflector.

To observe how this particular alternating arrangement affects the radiation pattern of the reflectarray, we carry out two independent runs of the GA. The optimization goal is to maximize the directivity at 45° and 65°, respectively, at 300 GHz. The design variables are the heights of the 67 reflectors, while the heights of the static reflectors are fixed at 300 μm. We choose the same GA option settings as in Section II. We also conduct full-wave EM simulations of the obtained reflectarrays. The calculated and EM simulated radiation patterns of the reflectarray are shown in Fig. 11. The calculated radiation patterns show little difference from the reflectarray with 80 actuated reflectors. However, we observe a slight degradation in the EM simulation results: the directivity in the target direction is 3 dB lower than the calculated value, and the sidelobe level around the normal of the reflectarray increases.

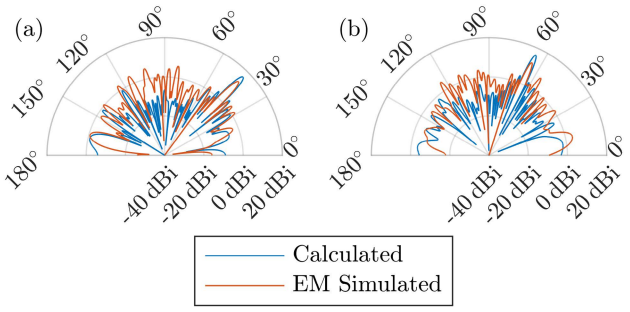

FIGURE 11. Calculated (in color blue) and EM simulated (in color red) radiation pattern of the reflectarray with the alternating arrangement obtained by GA with the objective of maximizing the directivity at the angle of (a) 45° and (b) 65°.

V. PROOF OF CONCEPT MEASUREMENT

To validate the proposed mathematical model and the feasibility of optimizing the MEMS-based reflectarray using a GA, we fabricate four reflectarray phantoms, i.e. reflectarrays without the MEMS actuation systems and measure their radiation patterns. Two of the reflectarray phantoms are the approximate blazed gratings. Their height profiles are designed to have diffraction angles of 56.4° and 41.8°, respectively, for the first grating order at 300 GHz. The height profiles of the other two reflectarray phantoms are determined by the GA. We want to compare the performance of the reflectarrays whose height profiles are generated by a GA with the performance of the grating structures. Therefore, the objective of the GA is to maximize the directivity at 300 GHz at the diffraction angles given above. In this section, we describe the fabrication process of the reflectarray phantoms, explain the radiation pattern measurement setup, and discuss the measurement results.

A. FABRICATION PROCESS OF THE REFLECTARRAY PHANTOMS

The fabrication of the reflectarray phantoms is performed on single side polished silicon wafer substrates with a diameter of 100 mm, and a thickness of 300 μm. The wafers are p-doped with a resistivity of 1-20 Ω·cm. The fabrication process is divided into two steps. In the first step, the single reflectors are fabricated. In the second step, the 80 single reflector chips are stacked together to form the reflectarray phantoms.

On the mask layout, each reflector has a 100 μm etching frame and an individual inscription to identify its geometry and simplify the stacking of the array. First, a 400 nm SiO_2 layer is deposited on the front and the back of the substrate by plasma-enhanced chemical vapor deposition (Fig. 12(a)). The SiO_2 layer on the front serves as an etching mask during deep reactive ion etch (DRIE) process. The layer on the back serves as a breakthrough barrier to prevent the cooling liquid on the carrying wafer to enter the etching trench. For lithography, an AZ MIR 701 29 cp coating is used (Fig. 12(b)). Then, the SiO_2 etching mask is etched (Fig. 12(c)) followed

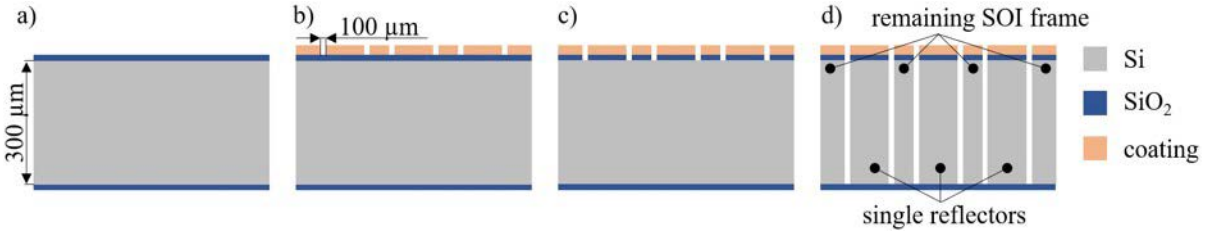

FIGURE 12. Flowchart of the fabrication process of the reflectarray phantom: (a)Si-substrate with 400 nm SiO_2 layer. (b) Lithography. (c) RIE of the SiO_2 etching mask. (d) DRIE of reflectors.

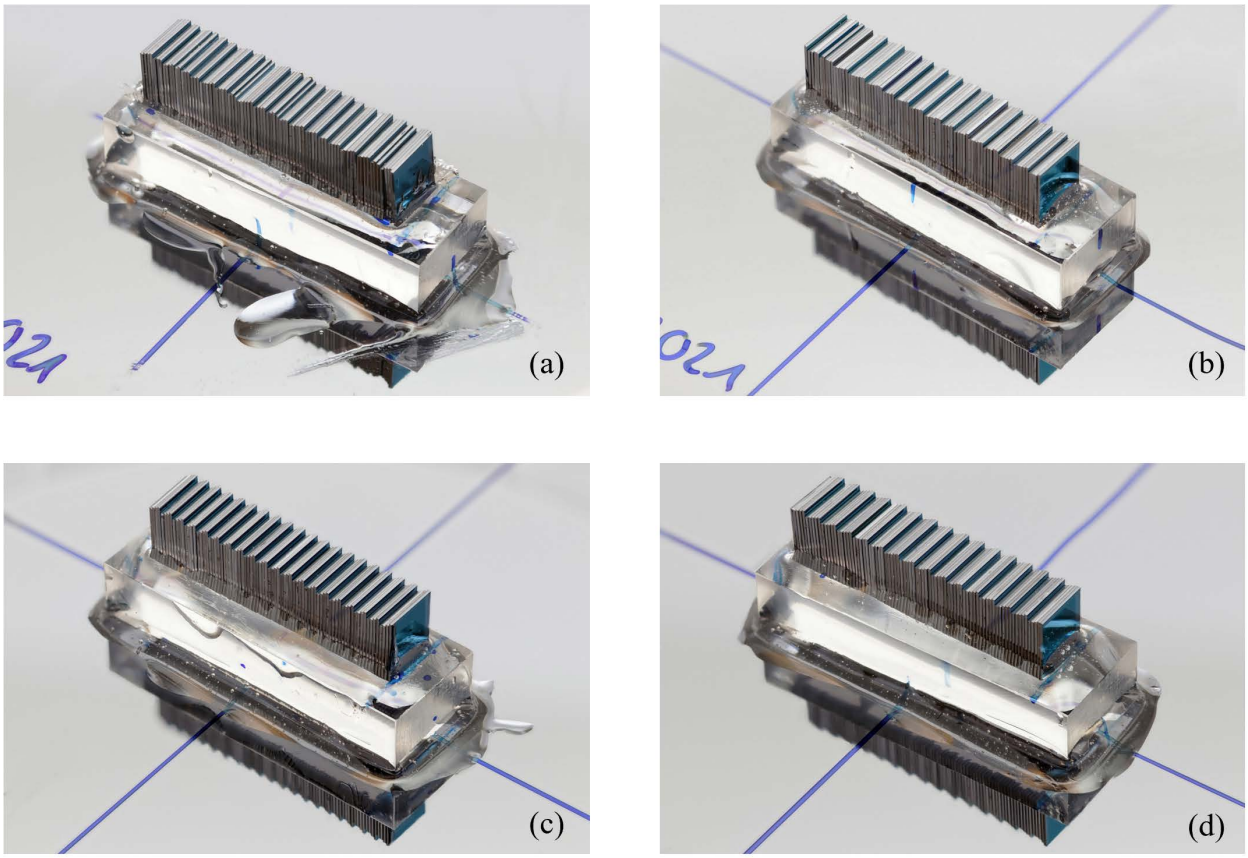

FIGURE 13. (a) Photograph of reflectarray phantom 1 whose height profile is generated by the GA. The objective of the GA is to maximize the directivity at 300 GHz at 56.4°. (b) Photograph of reflectarray phantom 2 whose height profile is generated by the GA. The objective of the GA is to maximize the directivity at 300 GHz at 41.8°. (c) Photograph of reflectarray phantom 3 which is an approximate blazed grating. Its height profile is designed to have diffraction angle of 56.4°. (d) Photograph of reflectarray phantom 4 which is an approximate blazed grating. Its height profile is designed to have diffraction angle of 41.8°.

by the DRIE process singularizing the chips (Fig. 12(d)). During DRIE, the substrate is placed on a carrying wafer. After DRIE, the chips are wet chemically cleaned and no additional metallization is performed. The reflective surface of the chips is comparable to the MEMS reflector used in the MEMS-based reflectarray.

In the second fabrication step, the chips are assorted, arranged, and aligned as straight as possible via adjustment aids. The fixation is performed with a commercially available two component adhesive. The stacked arrays are placed on an acrylic glass block with the lateral dimensions 30 mm × 10 mm, and a thickness of 6 mm. The acrylic glass block is fixed on a 3 inch carrying wafer substrate (Fig. 13).

B. PLANAR RADIATION PATTERN MEASUREMENT WITH A TERAHERTZ TDS SYSTEM

1) MEASUREMENT SETUP

We first carry out a planar radiation pattern measurement of the reflectarray phantoms with a terahertz time-domain spectroscopy (TDS) system. For the terahertz generation and detection, we use the fiber-coupled terahertz TDS system TERA K15 from Menlo Systems. The femtosecond fiber laser has a repetition rate of 100 MHz and a pulse duration of less than 90 fs. The terahertz spectrum typically has a spectral bandwidth of 5.5 THz and a peak dynamic range of 95 dB. The delay line of the system has a maximum delay of 1700 ps, which leads to a spectral resolution of 0.6 GHz.

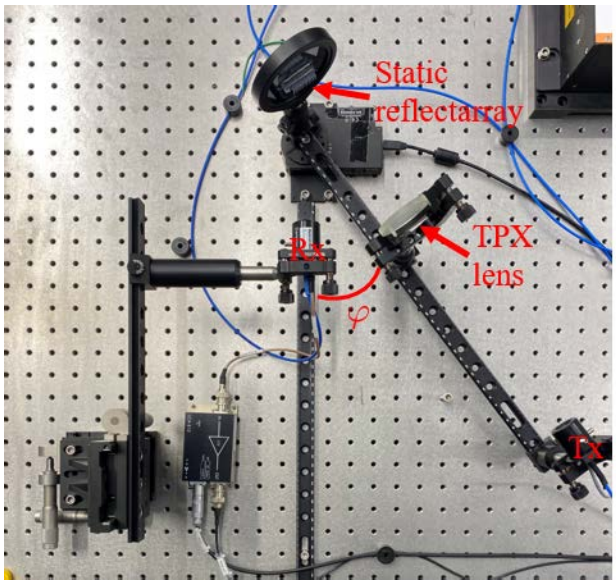

FIGURE 14. Planar radiation pattern measurement setup for the reflectarray phantom with the fiber-coupled terahertz TDS system.

The measurement setup is shown in Fig. 14. In this setup, the reflectarray phantom is rotated while the position of the terahertz receiver (Rx) remains fixed. To ensure a normally incident beam when the reflectarray phantom is rotated, we mount the terahertz transmitter (Tx) and a terahertz polymethylpentene (TPX) lens together with the reflectarray phantom on the same rail and fix the rail on a motorized rotation stage. The center of the reflectarray is aligned with the rotation center of the rotation stage. The terahertz lens we choose is a plano-convex TPX lens with a diameter of 2 inch and a long focal length of 250 mm so that the collimated beam (plane wave) can illuminate the entire reflectarray. The terahertz receiver is fixed on an *xyz*-stage and aligned to face the middle of the reflectarray. To avoid the collision between the terahertz receiver and the transmitted terahertz path, we set the rotation range between $\varphi = 15°$ and $\varphi = 65°$ in steps of 0.2°. At each angle, we take an average of 1000 measurements to improve the signal-to-noise power ratio. We set the scan window of the delay line to 200 ps, which is sufficient to capture the terahertz pulse with the adequate frequency resolution. The measurement duration for one reflectarray phantom is around 5 hours.

2) MEASUREMENT RESULTS

After obtaining the time-domain trace of the reflected terahertz pulse, the following signal processing is performed. We first multiply the time-domain trace with a Tukey window to eliminate the echoes and spurious signals while preserving the terahertz pulse. The windowed time-domain trace is then zero-padded so that its duration is equal to the temporal pulse spacing of the laser. Finally, the discrete Fourier transform is computed. The measured and calculated broadband radiation patterns for the four reflectarray phantoms at frequencies between 200 GHz and 800 GHz are shown in Fig. 15.

For all four reflectarray phantoms, the measured radiation patterns are in good agreement with the calculated ones. We also observe a frequency dependence of the main beams. Take reflectarray phantom 1 as an example. Its main beam approaches the normal of the reflectarray when the frequency increases from 260 GHz to 450 GHz. As explained in Section II-D, the reflectarray whose height profile is determined by the GA is a grating structure with a non-perfect period. This frequency dependence can then be explained by the grating equation. With increasing frequency (decreasing wavelength), the diffracted beam comes closer to the grating surface normal. By further increasing the frequency, we observe the second-order diffraction at frequencies between 520 GHz and 800 GHz.

Fig. 16 shows the radiation patterns of the four reflectarray phantoms at the design frequency of 300 GHz. The measured radiation patterns agree with the calculated ones in terms of the main lobe angle and side lobes angles. The maximum angular offset between the measured and calculated main beam directions is only about 2°. It can be attributed to the collimated beam not illuminating normally onto the reflectarray phantom due to misalignment. Furthermore, we observe higher sidelobe levels and broader main beamwidths in the measured radiation patterns compared with the calculated ones. The reason for this is that we do not place the terahertz receiver in the far field to ensure a sufficient dynamic range for the radiation pattern measurements.

C. 3D RADIATION PATTERN MEASUREMENT WITH A TERAHERTZ FDS SYSTEM

1) MEASUREMENT SETUP

To measure the partial hemispherical radiation patterns of the reflectarrays, we utilize a motorized spherical measurement system as shown in Fig. 17. The coverage of the measurement system is $0° \cdots 360°$ in azimuth and $0° \cdots 90°$ in elevation. We mount the reflectarray on a rail and fix it at the position where the center of the reflectarray is at the origin of the spherical system. The terahertz transmitter is attached on the same rail, facing the center of the reflectarray. The terahertz receiver is fixed on the arch frame and revolves around the measured reflectarray during the measurement. To avoid collisions between the terahertz transmitter and receiver, we set the elevation range of the measurement between 15° and 65°. Since the radiation patterns of the reflectarrays have a stronger angular dependence in elevation than in azimuth, we choose an elevation step size of 0.25° and an azimuth step size of 2°. We have in total 15972 angular points to measure. It would take around 22 days to finish measuring one reflectarray using the terahertz TDS system as mentioned in SectionV-B. Therefore, we use the terahertz frequency-domain spectroscopy system TeraScan 1550 from TOPTICA PHOTONICS, operating in the sampling mode at 300 GHz, to significantly reduce the measurement time to

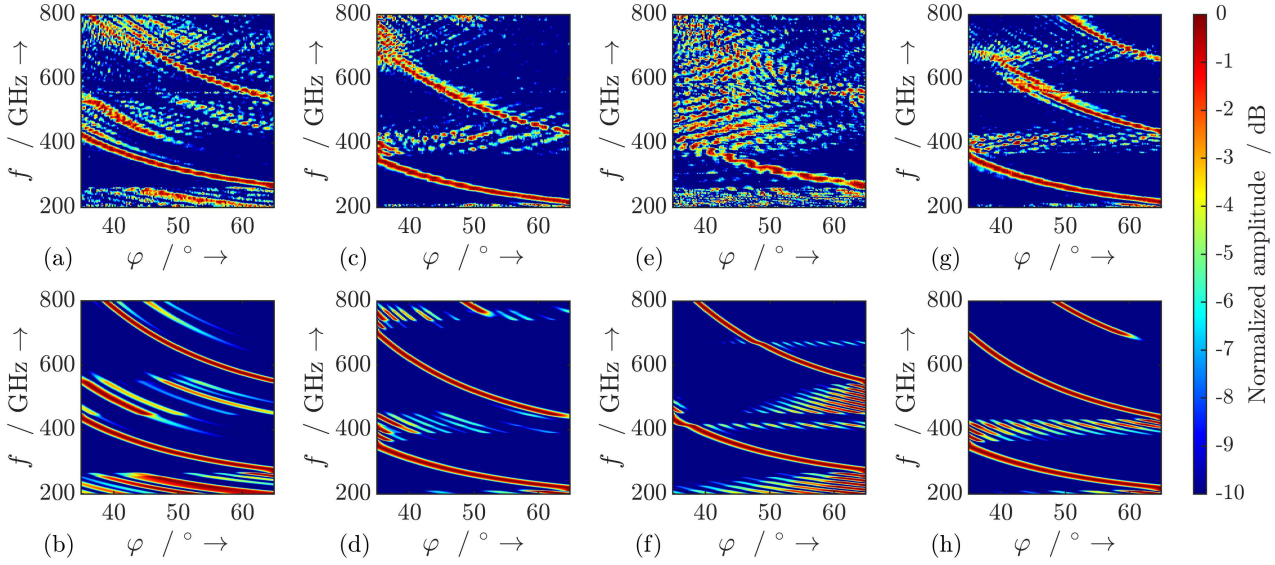

FIGURE 15. Measured broadband radiation pattern for the frequencies between 200 GHz and 800 GHz at the angles between 35° and 60° of (a) reflectarray phantom 1, (c) reflectarray phantom 2, (e) reflectarray phantom 3, and (g) reflectarray phantom 4. Calculated broadband radiation pattern for the frequencies between 200 GHz and 800 GHz at the angles between 35° and 60° of (b) reflectarray phantom 1, (d) reflectarray phantom 2, (f) reflectarray phantom 3, and (h) reflectarray phantom 4.

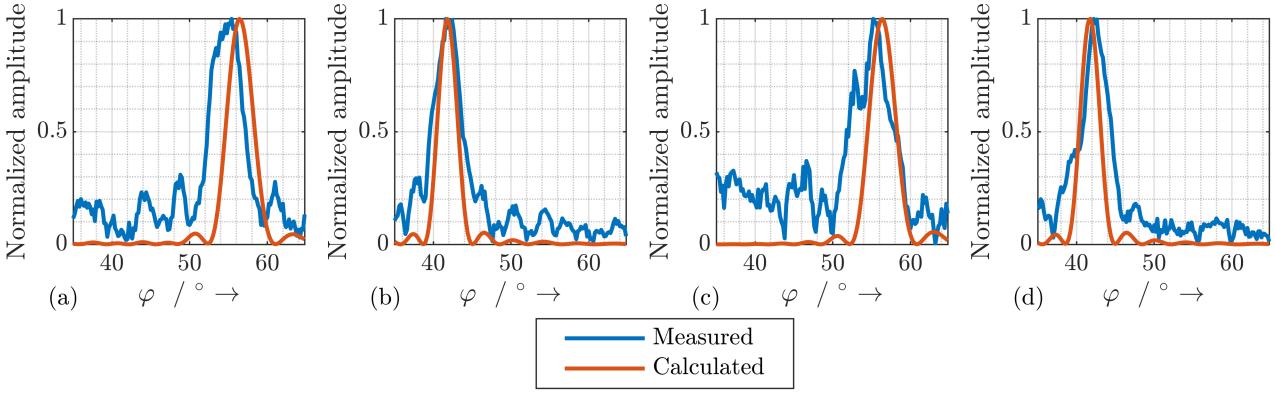

FIGURE 16. Measured (in color blue) and calculated (in color red) radiation pattern of (a) reflectarray phantom 1, (b) reflectarray phantom 2, (c) reflectarray phantom 3, and (d) reflectarray phantom 4 at 300 GHz.

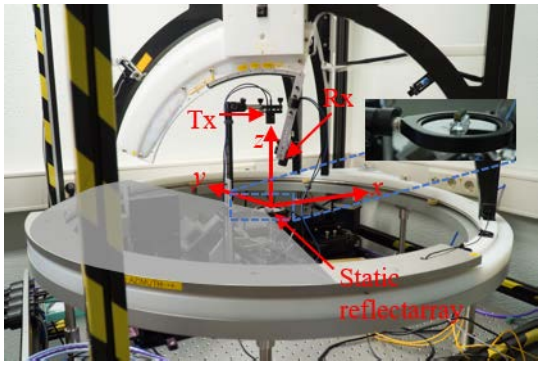

FIGURE 17. 3D radiation pattern measurement setup for the reflectarray phantom with the terahertz FDS system (gray shaded area is not measured).

7 hours. Another change we have to make in this measurement setup is to remove the collimating lens because we cannot accommodate the lens in this measurement setup while ensuring that the reflectarray phantom is placed in the center of the spherical measurement setup. As a result, the terahertz radiation illuminating directly onto the reflectarray phantom cannot be considered a strictly plane wave. We cannot subsequently interpret the measurement results quantitatively. However, with such measurements, we can still observe the relative differences between the reflectarrays whose height profiles are determined by the GA and the grating structure, as well as the relative differences between the elevation and azimuthal beamwidths.

2) MEASUREMENT RESULTS

The measured radiation patterns of the four reflectarrays are depicted in Fig. 18. For all four reflectarrays, we see a null around azimuth angle $\varphi = 0°$. This is due to the polarization mismatch between the terahertz transmitter and receiver. In addition, we also observe a strong reflection between elevation angle $\theta = 15°$ and $\theta = 30°$ caused by the specular reflection of the divergent terahertz beam on the silicon wafer.

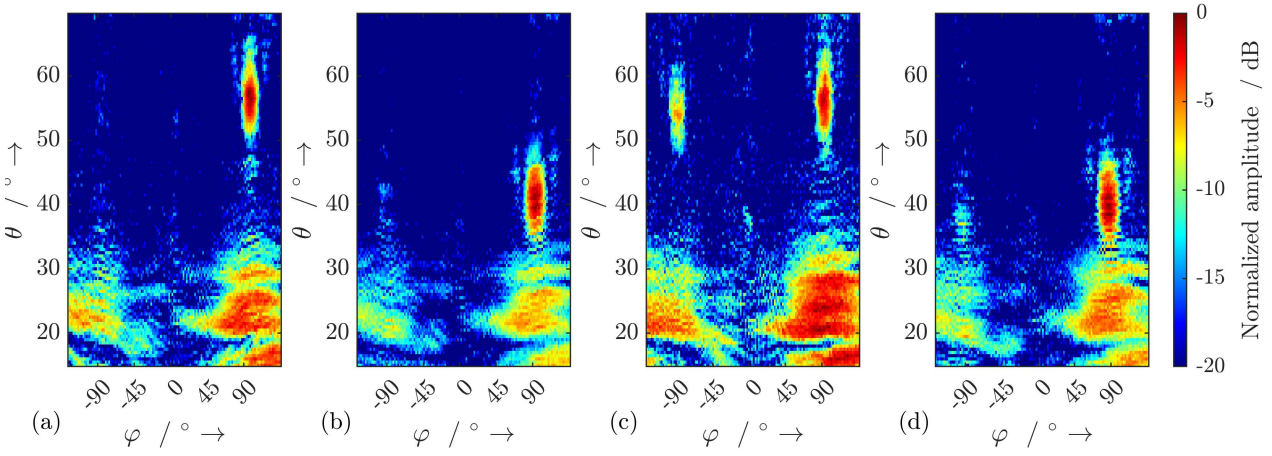

FIGURE 18. Measured 3D radiation pattern in elevation θ and in azimuth φ of (a) reflectarray phantom 1, (b) reflectarray phantom 2, (c) reflectarray phantom 3, and (d) reflectarray phantom 4 at the design frequency of 300 GHz.

TABLE 4. Performance comparison of different terahertz reflectarrays for beam steering.

Technique	Steering range at 300 GHz	Capability of a continuous steering	Presence of grating lobes	Capability of reducing the sidelobe level or nulling at a given angle
Binary grating [35]	40°	no	yes	no
Approximate blazed grating [38]	±56.4°	no	yes	no
Configuring the reflectarray using a GA (*This work*)	±90°	yes	no	yes

The main beams of the radiation patterns of four reflectarrays are in the target direction. The grating structures: reflectarray phantom 3 and 4 show grating lobes at the opposite side of their surface normal as expected, whereas the radiation patterns of reflectarray phantom 1 and 2 only have a main lobe in the target direction. The measured elevation and azimuth 3 dB-beamwidths of all four phantoms are around 5° and around 12°, respectively. This result reflects the fact that the reflectarray's electrical size is larger in the elevation than in the azimuth plane.

VI. CONCLUSION

In this work, we use a GA to optimize the radiation pattern of a MEMS-based reflectarray. The three optimization goals are to maximize the directivity in the target direction, minimize the sidelobe level, and place a null at a given angle. These objectives are first considered separately using a single-objective GA. We propose three different fitness functions for maximizing directivity and compare them numerically. Among them, the best fitness function yields a directivity of about 16.82 dBi. To minimize the sidelobe level, we also propose and numerically compare three different fitness functions. The GA with best fitness function returns the height profile of the reflectarray with a minimum sidelobe level of around -18.4 dB. Both calculated and EM simulated radiation patterns verify the feasibility of nulling at a given angle while keeping the main beam direction unchanged.

Realizing that the two optimization objectives of maximizing the directivity and minimizing the sidelobe level are conflicting, a multi-objective optimization is then carried out to determine the Pareto front: a set of optimal height profiles of the reflectarray that satisfies both objectives. By calculating the Fourier transform of the structure of the reflectarray obtained by the GA, we realize that the reflectarray obtained by the GA is a quasi-grating structure with a non-perfect period. We describe the structure of the reflectarray and the MEMS actuation mechanism in detail. We introduce an arrangement of the reflectarray by alternating the actuated reflectors and static reflectors to reduce the wire-bonding complexity.

Finally, as a proof of concept, we conduct planar and 3D radiation pattern measurements on each of the four reflectarray phantoms with terahertz TDS and FDS systems, respectively. For the planar radiation pattern, the measured broadband characteristics of all four reflectarray phantoms agree with the calculated results. The measured main beams at 300 GHz are in the designed direction with a maximum deviation of 2°. Comparing the measured 3D radiation patterns for four reflectarray phantoms, we see that the reflectarrays with height profiles determined by the GA are superior to grating structures, because they do not have grating lobes on the opposite side of the main beam. In Table 4, we compare the reflectarray configured by a GA with the other two terahertz reflectarrays in term of the beam steering performance.

It is clear from this work that using the GA to configure a reflectarray consisting of subwavelength reflectors is a better option than a reconfigurable grating structure for beam steering application. We anticipate that this concept can also be applied to optimize the geometrical arrangement, phase and amplitude distribution of terahertz phase arrays.

ACKNOWLEDGMENT

The authors acknowledge support by the Open Access Publication Fund of the University of Duisburg-Essen.

REFERENCES

[1] I. F. Akyildiz, J. M. Jornet, and C. Han, "Terahertz band: Next frontier for wireless communications," *Phys. Commun.*, vol. 12, pp. 16–32, Sep. 2014.

[2] A.-A. A. Boulogeorgos, A. Alexiou, T. Merkle, C. Schubert, R. Elschner, A. Katsiotis, P. Stavrianos, D. Kritharidis, P.-K. Chartsias, J. Kokkoniemi, M. Juntti, J. Lehtomaki, A. Teixeira, and F. Rodrigues, "Terahertz technologies to deliver optical network quality of experience in wireless systems beyond 5G," *IEEE Commun. Mag.*, vol. 56, no. 6, pp. 144–151, Jun. 2018.

[3] T. S. Rappaport, Y. Xing, O. Kanhere, S. Ju, A. Madanayake, S. Mandal, A. Alkhateeb, and G. C. Trichopoulos, "Wireless communications and applications above 100 GHz: Opportunities and challenges for 6G and beyond," *IEEE Access*, vol. 7, pp. 78729–78757, 2019.

[4] D. M. Mittleman, R. H. Jacobsen, R. Neelamani, R. G. Baraniuk, and M. C. Nuss, "Gas sensing using terahertz time-domain spectroscopy," *Appl. Phys. B, Lasers Opt.*, vol. 67, no. 3, pp. 379–390, Sep. 1998.

[5] J. Ornik, L. Heidrich, R. Schesny, E. Castro-Camus, C. M. Keck, and M. Koch, "Non-destructive crystallinity assessment of indomethacin in tablets made from smartfilms using terahertz time-domain spectroscopy," *Sci. Rep.*, vol. 12, no. 1, pp. 1–7, Apr. 2022.

[6] P. U. Jepsen, D. G. Cooke, and M. Koch, "Terahertz spectroscopy and imaging—Modern techniques and applications," *Laser Photon. Rev.*, vol. 5, no. 1, pp. 124–166, Jan. 2011.

[7] D. M. Mittleman, "Twenty years of terahertz imaging [invited]," *Opt. Exp.*, vol. 26, no. 8, pp. 9417–9431, Apr. 2018.

[8] D. Damyanov, I. Willms, J. C. Balzer, B. Friederich, M. Yahyapour, N. Vieweg, A. Deninger, K. Kolpatzeck, X. Liu, A. Czylwik, and T. Schultze, "High resolution lensless terahertz imaging and ranging," *IEEE Access*, vol. 7, pp. 147704–147712, 2019.

[9] L. Duvillaret, F. Garet, and J. L. Coutaz, "A reliable method for extraction of material parameters in terahertz time-domain spectroscopy," *IEEE J. Sel. Topics Quantum Electron.*, vol. 2, no. 3, pp. 739–746, Sep. 1996.

[10] H.-B. Liu, H. Zhong, N. Karpowicz, Y. Chen, and X.-C. Zhang, "Terahertz spectroscopy and imaging for defense and security applications," *Proc. IEEE*, vol. 95, no. 8, pp. 1514–1527, Aug. 2007.

[11] A. G. Davies, A. D. Burnett, W. Fan, E. H. Linfield, and J. E. Cunningham, "Terahertz spectroscopy of explosives and drugs," *Mater. Today*, vol. 11, no. 3, pp. 18–26, Mar. 2008.

[12] H. J. Liebe, T. Manabe, and G. A. Hufford, "Millimeter-wave attenuation and delay rates due to fog/cloud conditions," *IEEE Trans. Antennas Propag.*, vol. 37, no. 12, pp. 1612–1617, Dec. 1989.

[13] Y. Yang, A. Shutler, and D. Grischkowsky, "Measurement of the transmission of the atmosphere from 0.2 to 2 THz," *Opt. Exp.*, vol. 19, no. 9, pp. 8830–8838, Apr. 2011.

[14] D. Headland, Y. Monnai, D. Abbott, C. Fumeaux, and W. Withayachumnankul, "Tutorial: Terahertz beamforming, from concepts to realizations," *APL Photon.*, vol. 3, no. 5, May 2018, Art. no. 051101.

[15] X. Fu, F. Yang, C. Liu, X. Wu, and T. J. Cui, "Terahertz beam steering technologies: From phased arrays to field-programmable metasurfaces," *Adv. Opt. Mater.*, vol. 8, no. 3, Feb. 2020, Art. no. 1900628.

[16] K. Sengupta and A. Hajimiri, "A 0.28 THz power-generation and beam-steering array in CMOS based on distributed active radiators," *IEEE J. Solid-State Circuits*, vol. 47, no. 12, pp. 3013–3031, Dec. 2012.

[17] Y. Tousi and E. Afshari, "A scalable THz 2D phased array with +17 dBm of EIRP at 338 GHz in 65 nm bulk CMOS," in *IEEE Int. Solid-State Circuits Conf. (ISSCC) Dig. Tech. Papers*, Feb. 2014, pp. 258–259.

[18] Y. Yang, O. D. Gurbuz, and G. M. Rebeiz, "An eight-element 370–410-GHz phased-array transmitter in 45-nm CMOS SOI with peak EIRP of 8–8.5 dBm," *IEEE Trans. Microw. Theory Techn.*, vol. 64, no. 12, pp. 4241–4249, Dec. 2016.

[19] H.-T. Chen, W. J. Padilla, M. J. Cich, A. K. Azad, R. D. Averitt, and A. J. Taylor, "A metamaterial solid-state terahertz phase modulator," *Nature Photon.*, vol. 3, no. 3, pp. 148–151, Feb. 2009.

[20] P. Y. Chen, C. Argyropoulos, and A. Alù, "Terahertz antenna phase shifters using integrally-gated graphene transmission-lines," *IEEE Trans. Antennas Propag.*, vol. 61, no. 4, pp. 1528–1537, Apr. 2013.

[21] L. Wang, S. Ge, W. Hu, M. Nakajima, and Y. Lu, "Tunable reflective liquid crystal terahertz waveplates," *Opt. Mater. Exp.*, vol. 7, no. 6, pp. 2023–2029, 2017.

[22] X.-C. Wang, W.-S. Zhao, J. Hu, and W.-Y. Yin, "Reconfigurable terahertz leaky-wave antenna using graphene-based high-impedance surface," *IEEE Trans. Nanotechnol.*, vol. 14, no. 1, pp. 62–69, Jan. 2015.

[23] K. Murano, I. Watanabe, A. Kasamatsu, S. Suzuki, M. Asada, W. Withayachumnankul, T. Tanaka, and Y. Monnai, "Low-profile terahertz radar based on broadband leaky-wave beam steering," *IEEE Trans. THz Sci. Technol.*, vol. 7, no. 1, pp. 60–69, Jan. 2017.

[24] P. Lu, T. Haddad, B. Sievert, B. Khani, S. Makhlouf, S. Dulme, J. F. Estévez, A. Rennings, D. Erni, U. Pfeiffer, and A. Stöhr, "InP-based THz beam steering leaky-wave antenna," *IEEE Trans. THz Sci. Technol.*, vol. 11, no. 2, pp. 218–230, Mar. 2021.

[25] M. Esquius-Morote, J. S. Gómez-Díaz, and J. Perruisseau-Carrier, "Sinusoidally modulated graphene leaky-wave antenna for electronic beamscanning at THz," *IEEE Trans. THz Sci. Technol.*, vol. 4, no. 1, pp. 116–122, Jan. 2014.

[26] M. R. M. Hashemi, S.-H. Yang, T. Wang, N. Sepúlveda, and M. Jarrahi, "Electronically-controlled beam-steering through vanadium dioxide metasurfaces," *Sci. Rep.*, vol. 6, no. 1, Dec. 2016, Art. no. 35439.

[27] P. Ding, Y. Li, L. Shao, X. Tian, J. Wang, and C. Fan, "Graphene aperture-based metalens for dynamic focusing of terahertz waves," *Opt. Exp.*, vol. 26, no. 21, pp. 28038–28050, Oct. 2018.

[28] Z. Tan, F. Fan, X. Dong, J. Cheng, and S. Chang, "Nonreciprocal terahertz beam steering based on magneto-optic metagratings," *Sci. Rep.*, vol. 9, no. 1, Dec. 2019, Art. no. 20210.

[29] S. Preu, S. Malzer, G. H. Döhler, J. Zhang, Z. H. Lu, and L. J. Wang, "Highly collimated and directional continous-wave terahertz emission by photomixing in semiconductor device arrays," *Proc. SPIE*, vol. 6194, Apr. 2006, Art. no. 61940F.

[30] K. Maki and C. Otani, "Terahertz beam steering and frequency tuning by using the spatial dispersion of ultrafast laser pulses," *Opt. Exp.*, vol. 16, no. 14, pp. 10158–10169, 2008.

[31] S. Busch, B. Scherger, M. Scheller, and M. Koch, "Optically controlled terahertz beam steering and imaging," *Opt. Lett.*, vol. 37, no. 8, pp. 1391–1393, 2012.

[32] X. Wang, Z. Xie, W. Sun, S. Feng, Y. Cui, J. Ye, and Y. Zhang, "Focusing and imaging of a virtual all-optical tunable terahertz Fresnel zone plate," *Opt. Lett.*, vol. 38, no. 22, pp. 4731–4734, 2013.

[33] T. P. Steinbusch, H. K. Tyagi, M. C. Schaafsma, G. Georgiou, and J. G. Rivas, "Active terahertz beam steering by photo-generated graded index gratings in thin semiconductor films," *Opt. Exp.*, vol. 22, no. 22, pp. 26559–26571, 2014.

[34] A. Kannegulla, M. I. B. Shams, L. Liu, and L. Cheng, "Photo-induced spatial modulation of THz waves: Opportunities and limitations," *Opt. Exp.*, vol. 23, no. 25, pp. 32098–32112, 2015.

[35] Y. Monnai, K. Altmann, C. Jansen, H. Hillmer, M. Koch, and H. Shinoda, "Terahertz beam steering and variable focusing using programmable diffraction gratings," *Opt. Exp.*, vol. 21, no. 2, pp. 2347–2354, Jan. 2013.

[36] K. M. Schmitt and M. Rahm, "Evaluation of the impact of diffraction on image reconstruction in single-pixel imaging systems," *Opt. Exp.*, vol. 24, no. 21, pp. 23863–23871, 2016.

[37] J. Kappa, K. M. Schmitt, and M. Rahm, "Electromagnetic behavior of spatial terahertz wave modulators based on reconfigurable micromirror gratings in Littrow configuration," *Opt. Exp.*, vol. 25, no. 17, pp. 20850–20859, 2017.

[38] X. Liu, L. Samfaß, K. Kolpatzeck, L. Häring, J. C. Balzer, M. Hoffmann, and A. Czylwik, "Terahertz beam steering concept based on a MEMS-reconfigurable reflection grating," *Sensors*, vol. 20, no. 10, p. 2874, May 2020.

[39] A. Sheikholeslami and Z. Atlasbaf, "Novel phase distributions for large electronically beam-scanning reflectarrays," *Sci. Rep.*, vol. 11, no. 1, pp. 1–15, Dec. 2021.

[40] L. Schmitt, P. Schmitt, and M. Hoffmann, "3-bit digital-to-analog converter with mechanical amplifier for binary encoded large displacements," *Actuators*, vol. 10, no. 8, p. 182, Aug. 2021.

[41] R. Legtenberg, A. W. Groeneveld, and M. Elwenspoek, "Comb-drive actuators for large displacements," *J. Micromech. Microeng.*, vol. 6, no. 3, p. 320, 1996.

[42] J. D. Grade, H. Jerman, and T. W. Kenny, "Design of large deflection electrostatic actuators," *J. Microelectromech. Syst.*, vol. 12, no. 3, pp. 335–343, Jun. 2003.

[43] G. Xue, M. Toda, and T. Ono, "Assembled comb-drive XYZ-microstage with large displacements for low temperature measurement systems," in *Proc. 28th IEEE Int. Conf. Micro Electro Mech. Syst. (MEMS)*, Jan. 2015, pp. 14–17.
[44] P. Edinger, A. Y. Takabayashi, C. Errando-Herranz, U. Khan, H. Sattari, P. Verheyen, W. Bogaerts, N. Quack, and K. B. Gylfason, "Silicon photonic microelectromechanical phase shifters for scalable programmable photonics," *Opt. Lett.*, vol. 46, no. 22, pp. 5671–5674, Nov. 2021.
[45] X. Zhao, K. Fan, J. Zhang, G. R. Keiser, G. Duan, R. D. Averitt, and X. Zhang, "Voltage-tunable dual-layer terahertz metamaterials," *Microsyst. Nanoeng.*, vol. 2, no. 1, Dec. 2016, Art. no. 16025.
[46] L. Schmitt and M. Hoffmann, "Large stepwise discrete microsystem displacements based on electrostatic bending plate actuation," *Actuators*, vol. 10, no. 10, Oct. 2021, Art. no. 272.
[47] R. Yeh, R. A. Conant, and K. S. J. Pister, "Mechanical digital-to-analog converters," in *Proc. 10th Int. Solid-State Sens. Actuators Conf.*, Sendai, Japan, 1999, pp. 998–1001.
[48] Q. Liu and Q. A. Huang, "Design and finite element analysis of weighted-stiffness microelectromechanical digital-to-analogue converters," *Electron. Lett.*, vol. 37, no. 12, pp. 755–756, 2001.
[49] P. Pandiyan, G. Uma, and M. Umapathy, "Design and simulation of MEMS-based digital-to-analog converters for in-plane actuation," *Arabian J. Sci. Eng.*, vol. 42, no. 12, pp. 4991–5001, Dec. 2017.
[50] H. Toshiyoshi, D. Kobayashi, M. Mita, G. Hashiguchi, H. Fujita, J. Endo, and Y. Wada, "Microelectromechanical digital-to-analog converters of displacement for step motion actuators," *J. Microelectromech. Syst.*, vol. 9, no. 2, pp. 218–225, 2000.
[51] E. Sarajlic, D. Collard, H. Toshiyoshi, and H. Fujita, "Design and modeling of compliant micromechanism for mechanical digital-to-analog conversion of displacement," *IEEJ Trans. Electr. Electron. Eng.*, vol. 2, no. 3, pp. 357–364, 2007.
[52] P. Schmitt and M. Hoffmann, "Engineering a compliant mechanical amplifier for MEMS sensor applications," *J. Microelectromech. Syst.*, vol. 29, no. 2, pp. 214–227, Apr. 2020.
[53] L. Schmitt, X. Liu, A. Czylwik, and M. Hoffmann, "Design and fabrication of MEMS reflectors for THz reflect-arrays," in *Proc. 4th Int. Workshop Mobile THz Syst. (IWMTS)*, Jul. 2021, pp. 1–5.

XUAN LIU received the B.Sc. degree in electrical and electronic engineering and the M.Sc. degree in communications engineering from the University of Duisburg-Essen, in 2015 and 2017, respectively, where she is currently pursuing the Ph.D. degree. Since 2018, she has been working as a Research Associate with the Chair of Communication Systems, University of Duisburg-Essen, within the Collaborative Research Center MARIE with an aim of obtaining the Ph.D. degree. Her research interests include terahertz system development and passive terahertz components focusing at beam steering and beamforming.

LISA SCHMITT received the M.S. degree in industrial engineering from Technische Universität Ilmenau, Germany, in 2018. From 2018 to 2019, she has worked as a Research Assistant with the Department of Material Test Engineering, TU Dortmund, Germany. Since 2019, she has been continuing her research with Ruhr-Universität Bochum, Germany, with focus on large displacement and multi-stable MEMS actuators and MEMS-based devices to be integrated in THz systems.

BENEDIKT SIEVERT (Member, IEEE) was born in Krefeld, Germany. He received the B.Sc. and M.Sc. degrees in electrical engineering/high-frequency systems from the University of Duisburg-Essen, in 2017 and 2019, respectively. Since 2017, he has been a member with the Laboratory of General and Theoretical Electrical Engineering, University of Duisburg-Essen. His research interests include mm-wave on-chip antennas, electromagnetic metamaterials, and theoretical and computational electromagnetics.

JONAS LIPKA was born in Wesel, Germany, in 1998. He received the B.Sc. degree in electrical engineering and information technology from the University of Duisburg-Essen, in 2022. His bachelor's thesis covered the topic of configuration of a MEMS-based reflector array using the GA for terahertz beamforming.

CHONG GENG was born in Hebei, China, in 1993. She received the B.Sc. degree in electrical and electronic engineering and the M.Sc. degree in communications engineering from the University of Duisburg-Essen, Germany, in 2018 and 2022, respectively. Her master's thesis is about the broadband characterization of a Mach-Zehnder-modulator-based optical ring resonator.

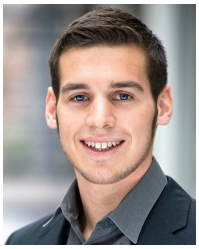

KEVIN KOLPATZECK received the B.S., M.S., and Ph.D. degrees in electrical engineering and information technology from the University of Duisburg-Essen, Germany, in 2013, 2016, and 2022, respectively.

He has investigated terahertz time-domain spectroscopy systems driven by monolithic mode-locked laser diodes at the University of Duisburg-Essen. He is currently a Postdoctoral Researcher with the Chair of Communication Systems (NTS), University of Duisburg-Essen. His current research interests include terahertz photonics, beamforming at terahertz frequencies, and the use of terahertz technology in radar applications as well as non-destructive testing.

DANIEL ERNI (Member, IEEE) received the Diploma degree in electrical engineering from the University of Applied Sciences Rapperswil (OST), Rapperswil, Switzerland, in 1986, and the Diploma degree in electrical engineering and the Ph.D. degree in laser physics from ETH Zürich, Zürich, Switzerland, in 1990 and 1996, respectively. From 1995 to 2006, he was the Founder and the Head of the Communication Photonics Group, ETH Zürich, where he has been with the Laboratory for Electromagnetic Fields and Microwave Electronics (IFH), since 1990. Since October 2006, he has been a Full Professor with the Department of General and Theoretical Electrical Engineering, University of Duisburg-Essen, Duisburg, Germany. From 2017 to 2018, he was with

the Institute of Electromagnetic Fields (IEF), ETH Zürich, as a Visiting Professor. He is currently a Co-Founder of spin-off company airCode, Hamm, Germany, working on flexible printed RFID technology. His current research interests include optical interconnects, nanophotonics, plasmonics, advanced solar cell concepts, optical and electromagnetic metamaterials, RF, mm-wave and THz engineering, chipless flexible RFIDs, biomedical engineering, bioelectromagnetics, marine electromagnetics, computational electromagnetics, multiscale and multiphysics modeling, numerical structural optimization, and science and technology studies (STS). He is a fellow of The Electromagnetics Academy and a member of the Center for Nanointegration Duisburg-Essen (CeNIDE), as well as of Materials Chain, the Flagship Program of University Alliance Ruhr, the Swiss Physical Society (SPS), German Physical Society (DPG), and the Optical Society of America (OSA).

ANDREAS RENNINGS (Member, IEEE) received the Dipl.-Ing. and Dr.-Ing. degrees from the University of Duisburg-Essen, Germany, in 2000 and 2008, respectively. He carried out his Diploma work during a stay at the University of California at Los Angeles. He studied electrical engineering at the University of Duisburg-Essen. From 2006 to 2008, he was with IMST GmbH, Kamp-Lintfort, Germany, where he has worked as an RF Engineer. Since then, he has been a Senior Scientist and the Principal Investigator at the Laboratory for General and Theoretical Electrical Engineering, University of Duisburg-Essen. His general research interests include all aspects of theoretical and applied electromagnetics, currently with a focus on medical applications and on-chip millimeter-wave/THz antennas. He has received several awards, including the Student Paper Price at the 2005 IEEE Antennas and Propagation Society International Symposium and the VDE-Promotionspreis 2009 for the dissertation.

JAN C. BALZER (Member, IEEE) received the Dipl.-Ing. (FH) degree in telecommunications from the Dortmund University of Applied Sciences, Germany, in 2008, and the Master of Science degree in electrical engineering and information technology and the Dr.-Ing. degree from Ruhr University Bochum, Bochum, Germany, in 2010 and 2014, respectively. In 2015, he has joined the esearch group of Prof. Martin Koch, Philipp University of Marburg, Marburg, Germany, as a Postdoctoral Fellow. Since 2017, he has been an Assistant Professor for terahertz systems at the Faculty of Engineering, University of Duisburg-Essen, Germany. His scientific interest includes ultrafast semiconductor lasers. From here, he moved to the field of terahertz radiation generation and applications. He made contributions in the field of compact laser diode-driven THz systems, 3D-printed THz devices, high-resolution THz imaging, and THz material characterization.

MARTIN HOFFMANN received the Ph.D. degree from Technische Universität Dortmund, in 1996. After years in academic research and industry, he joined Technische Universität Ilmenau and took over the Chair of micromechanical systems. In 2017, he moved to Ruhr-Universität Bochum and currently heads the Chair of Microsystems Technology. His research interests include actuators and passive sensor systems based on micromechanics.

ANDREAS CZYLWIK received the Dr.-Ing. and Habilitation degrees in optical communications from the Technical University of Darmstadt, Germany, in 1988 and 1994, respectively.

He has studied electrical engineering at the Technical University of Darmstadt, from 1978 to 1983. From 1994 to 2000, he was with the Research and Development Center (Technologiezentrum) of the Department of Local Area Broadband Radio Systems, Deutsche Telekom. In 2000, he became a Full Professor at the Technical University of Braunschweig, heading the Research Group of Microcellular Radio Systems. Since 2002, he has been with the University of Duisburg-Essen, heading the Chair of Communication Systems. His research interests include radio communications on link and system level with special focus on adaptive multicarrier MIMO techniques. His several research activities focus on utilizing high frequency (up to THz) electromagnetic waves with applications in the field of extreme wideband communications and radar systems. He is also interested in the application of radio communications in the field of technical security systems.

Dr. Czylwik has been the Chairperson of EUSAS and the European Society for Automatic Alarm Systems, since 2014.